

Article

# UV-Visible-Near-Infrared-Driven Photoelectrocatalytic Urea Oxidation and Photocatalytic Urea Fuel Cells Based on Ruddlensden–Popper-Type Perovskite Oxide $\text{La}_2\text{NiO}_4$

Mingwen Xiong<sup>1,\*</sup>, Ying Tao<sup>2,†</sup>, Lanlan Fu<sup>2</sup>, Donglai Pan<sup>3</sup>, Yuxin Shi<sup>2</sup>, Tong Hu<sup>1</sup>, Jiayu Ma<sup>1</sup>, Xiaofeng Chen<sup>2,\*</sup> and Guisheng Li<sup>2,3,\*</sup><sup>1</sup> School of Materials and Chemical Engineering, Bengbu University, Bengbu 233030, China<sup>2</sup> School of Environmental and Geographical Sciences, Wetland Ecosystem Observation and Research Field Station, Shanghai Normal University, Shanghai 200234, China<sup>3</sup> Key Laboratory of Resource Chemistry of Ministry of Education, Shanghai Normal University, Shanghai 200234, China

\* Correspondence: xiongmw@163.com (M.X.); xiaofengchen@shnu.edu.cn (X.C.); liguisheng@shnu.edu.cn (G.L.)

† These authors contributed equally to this work.

**Abstract:** Photocatalysis and photoelectrocatalysis, as green and low-cost pollutant treatment technologies, have been widely used to simultaneously degrade pollutants and produce clean energy to solve the problems of environmental pollution and energy crisis. However, the disadvantages of photocatalysts in a narrow absorption range and low utilization rate of solar energy still hinder the practical application. Here we fabricate two-dimensional porous Ruddlensden–Popper type nickel-based perovskite oxide  $\text{La}_2\text{NiO}_4$  as a noble metal-free photoanode for photoelectrocatalytic urea oxidation under full spectrum sunlight irradiation. The transient photocurrent density under near infrared (NIR) light ( $\lambda > 800$  nm) can reach  $50 \mu\text{A cm}^{-2}$ . Urea wastewater was used as the fuel to obtain low-energy hydrogen production, and round-the-clock hydrogen production was achieved with the optimal yield of  $22.76 \mu\text{mol cm}^{-2} \text{ h}^{-1}$ . Moreover, a photocatalytic urea fuel cell (PUFC) was constructed with  $\text{La}_2\text{NiO}_4$  as the photoanode. The power density under UV-vis-NIR was  $0.575 \mu\text{W cm}^{-2}$ . Surprisingly, the filling factor (FF) under NIR light was 0.477, which was much higher than those under UV-vis-NIR and visible light. The results demonstrated that PUFCs constructed from low-cost nickel-based perovskite oxides have potential applications for low-energy hydrogen production and efficient utilization of sunlight.

**Keywords:** round-the-clock; near-infrared light; photoelectrocatalysis; urea oxidation reaction; photocatalytic urea fuel cell;  $\text{La}_2\text{NiO}_4$



**Citation:** Xiong, M.; Tao, Y.; Fu, L.; Pan, D.; Shi, Y.; Hu, T.; Ma, J.; Chen, X.; Li, G. UV-Visible-Near-Infrared-Driven Photoelectrocatalytic Urea Oxidation and Photocatalytic Urea Fuel Cells Based on Ruddlensden–Popper-Type Perovskite Oxide  $\text{La}_2\text{NiO}_4$ . *Catalysts* **2023**, *13*, 53. <https://doi.org/10.3390/catal13010053>

Academic Editor: Barbara Mecheri

Received: 24 November 2022

Revised: 16 December 2022

Accepted: 20 December 2022

Published: 27 December 2022



**Copyright:** © 2022 by the authors. Licensee MDPI, Basel, Switzerland. This article is an open access article distributed under the terms and conditions of the Creative Commons Attribution (CC BY) license (<https://creativecommons.org/licenses/by/4.0/>).

## 1. Introduction

With fast industrialization and urbanization, urea, one of the most common pollutants in wastewater, inevitably produces a mass of ammonia and nitrate under natural degradation, which poses severe risks to the environment and public health [1]. Thus, it is of great significance to develop cost-effective ways for urea removal in wastewater [2]. Meanwhile, urea is widely recognized as an efficient material for  $\text{H}_2$  transportation and storage due to its high energy density ( $16.9 \text{ MJ L}^{-1}$ ) [3]. Compared with electrolytic water (1.23 V vs. RHE), electrolytic urea solution shows a relatively lower theoretical electrolytic voltage (0.37 V vs. RHE), which is beneficial for electrolytic  $\text{H}_2$  production from wastewater containing urea [4–7]. The largest source of urea is urine discharge from humans and livestock. The high concentration of urea in human urine ( $\sim 0.33 \text{ M}$ ) has been extensively utilized to produce hydrogen and to directly construct urine fuel cells [8–12].

Photoelectrocatalysis is regarded as a promising technology for urea wastewater treatment and  $\text{H}_2$  production, due to its high efficiency in solar energy utilization [13–21].

Li et al. reported the photoelectrocatalytic oxidation of urea with Ni(OH)<sub>2</sub> modified TiO<sub>2</sub> as the photoelectrode, for the first time, in 2012, which aroused great interest in solar-driven hydrogen released from urea and human urine [22]. Xie et al. further improved the photoelectrochemical oxidation activity of urea by using a Ni(OH)<sub>2</sub>-modified Ti-doped  $\alpha$ -Fe<sub>2</sub>O<sub>3</sub> photoanode [23]. However, conventional photocatalysts (TiO<sub>2</sub>,  $\alpha$ -Fe<sub>2</sub>O<sub>3</sub>, BiVO<sub>4</sub> etc.) have a narrow solar absorption band, which greatly restricts utilization of solar energy [24,25]. Currently, there are only a few reports on urea oxidation reaction (UOR) by photoelectrocatalysts that utilizes the entire solar spectrum (from UV to NIR region), especially NIR light [26–28]. Therefore, the development of a cheap transition metal-based photoelectrode, with broad spectrum response, is crucial for cost-effective urea wastewater treatment and clean energy conversion via photoelectrocatalytic technology.

It is well known that the efficiency of urea oxidation depends on the rate of the anodic urea oxidation reaction [11,29,30]. However, UOR is a kinetically slow process which involves 6e<sup>-</sup> transfer [31,32]. Therefore, using a high-performance photoelectrocatalyst to reduce the UOR overpotential is the key to accelerate the kinetics. Nickel-based catalysts have been extensively developed for urea electrolysis, since they can effectively reduce the active potential of UOR [3,32–34]. Among nickel-based catalysts, perovskite oxides are the most attractive, due to their adjustable composition, as well as excellent light absorption ability [5,35–39]. Perovskite oxides are generally prepared under high temperature conditions, resulting in less active sites on the surface and low activity [40–43]. Thus, improving the active sites on the surface of nickel-based perovskite oxides is very important to enhance the performance of solar-driven urea oxidation, and realize the treatment and energy conversion of urea wastewater.

Herein, we employed rGO as a template to successfully prepare a two-dimensional porous Ruddlesden–Popper La<sub>2</sub>NiO<sub>4</sub> perovskite with abundant active sites on the surface for photoelectrocatalytic urea oxidation [44]. The photocurrent densities of the obtained La<sub>2</sub>NiO<sub>4</sub> photoanode, at a potential of 1.47 V vs. RHE, were 2.94, 2.50 and 2.00 mA cm<sup>-2</sup> under UV-vis-NIR, visible, and NIR light irradiation, respectively. Moreover, the corresponding photocatalytic urea fuel cells (PUFCs) were adopted to show the great potential of the two-dimensional porous La<sub>2</sub>NiO<sub>4</sub> for practical urea wastewater treatment. Under NIR irradiation, both the urea solution and real human urine showed a large filling factor (FF) of 0.477 and 0.411 with maximum power densities (P<sub>max</sub>) of 0.129  $\mu$ W cm<sup>-2</sup> and 0.041  $\mu$ W cm<sup>-2</sup>, respectively. The results demonstrated that the La<sub>2</sub>NiO<sub>4</sub> photoanode showed full spectral response to efficiently oxidize urea solution.

## 2. Results and Discussion

### 2.1. Preparation and Characterizations of Catalysts

The holey two-dimensional La<sub>2</sub>NiO<sub>4</sub> nanosheets were fabricated using rGO as a sacrificial template through a general two-step strategy, as schematically illustrated in Figure 1. The starting La<sub>2</sub>NiO<sub>4</sub> precursor, grown on rGO, was obtained through the chemical impregnation treatment of the starting materials [44]. The X-ray diffraction (XRD) pattern of the La<sub>2</sub>NiO<sub>4</sub> precursor/rGO revealed an amorphous structure, since no diffraction peaks were found (Figure S1). Subsequently, we annealed the La<sub>2</sub>NiO<sub>4</sub> precursor/rGO under air at 400 °C to remove the rGO template, and, further, at 800 °C to give pure La<sub>2</sub>NiO<sub>4</sub> (Figure 1). As shown in Figure 2a, both a Ruddlesden–Popper La<sub>2</sub>NiO<sub>4</sub> phase (PDF#34-0314) and a small amount of La<sub>2</sub>O<sub>3</sub> (PDF#05-0602) were observed. The general formula for the Ruddlesden–Popper phase is described as A<sub>n+1</sub>B<sub>n</sub>O<sub>3n+1</sub> or A<sub>2</sub>'A<sub>n-1</sub>B<sub>n</sub>O<sub>3n+1</sub>, which is constructed of a LaNiO<sub>3</sub> perovskite unit and a LaO rock salt unit (top right inset of Figure 2a) [44]. The morphology was of two-dimensional nanosheets with a holey feature inherited from rGO (Figure 2b–e and Figure S2). The diffused concentric rings in the selected area electron diffraction (SAED) pattern (inset of Figure 2d) indicated a polycrystalline feature. The clear lattice fringes were determined to be 0.273 nm, which corresponded well to the (110) facet of the tetragonal La<sub>2</sub>NiO<sub>4</sub> (Figure 2e). The SEM-EDS mapping images revealed that the obtained La<sub>2</sub>NiO<sub>4</sub> nanosheets were principally

composed of La, Ni, and O, with a uniform spatial distribution (Figure 2c). The Brunauer–Emmett–Teller (BET) surface area of the holey  $\text{La}_2\text{NiO}_4$  nanosheets ( $14.0 \text{ m}^2 \text{ g}^{-1}$ ) was much higher than that of the sample obtained without the rGO template ( $5.6 \text{ m}^2 \text{ g}^{-1}$ ) (Figure S3). These results demonstrated that the application of rGO as a template could dramatically increase the BET surface area of  $\text{La}_2\text{NiO}_4$ , and, thus, increase the reactive sites. The holey two-dimensional nanosheet structure could also enhance light reflection and improve the reactivity of UOR (Figure S4).

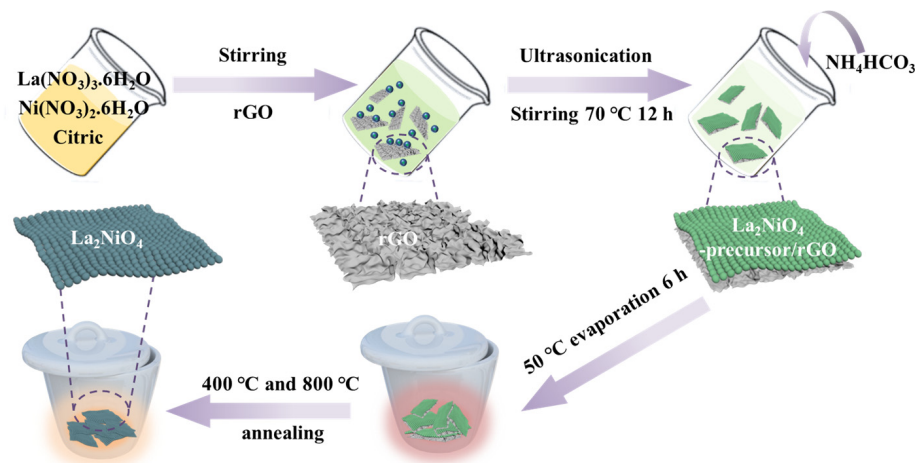


**Figure 1.** Schematic illustration of the preparation of  $\text{La}_2\text{NiO}_4$  as a UOR catalyst. (The green and dark green balls represent  $\text{La}_2\text{NiO}_4$  precursor and  $\text{La}_2\text{NiO}_4$ , respectively).

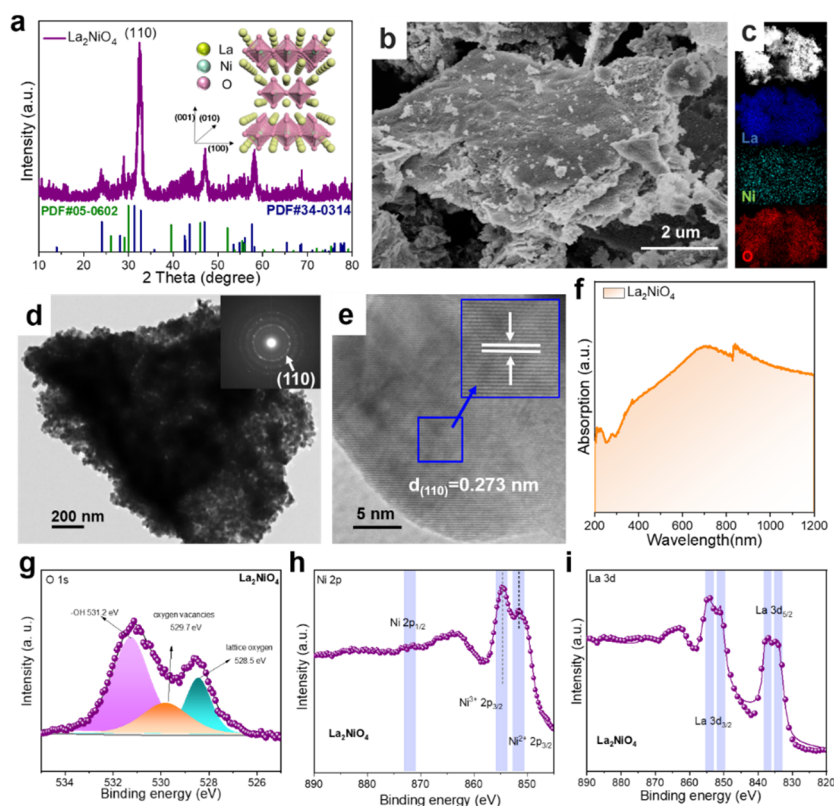


**Figure 2.** (a) XRD patterns of  $\text{La}_2\text{NiO}_4$ . (b–e) SEM, SEM-EDS mapping, TEM and HRTEM images of  $\text{La}_2\text{NiO}_4$ . The insets in (d) show the corresponding SAED patterns. UV-vis absorption spectra (f) of  $\text{La}_2\text{NiO}_4$ . XPS spectra of (g) O 1s, (h) Ni 2p, and (i) La 3d for obtained  $\text{La}_2\text{NiO}_4$ .

The UV–vis–NIR diffuse reflectance spectra showed that  $\text{La}_2\text{NiO}_4$  exhibited broad spectral absorption that covered near-infrared (NIR) light ( $\lambda = 200\text{--}1200\text{ nm}$ ) (Figure 2f), which indicated that the material had potential photocatalysis activities under NIR light irradiation. The absorbance decreased with increasing of the annealing temperature, which might be caused by the reduction of light reflection, due to the reduction of pores (Figure S5a). Typical diffraction peaks of perovskite oxide  $\text{La}_2\text{NiO}_4$ , with a spinel structure (PDF#34-0314), and a small amount of  $\text{La}_2\text{O}_3$  (PDF#05-0602) were observed for the samples annealed at  $700\text{ }^\circ\text{C}$ ,  $800\text{ }^\circ\text{C}$  and  $900\text{ }^\circ\text{C}$ . However, the diffraction peak of the spinel structure was obviously enhanced and became sharper, and no peak of impurities was found when the annealing temperature was  $1000\text{ }^\circ\text{C}$ , indicating that the sample obtained was composed of pure  $\text{La}_2\text{NiO}_4$  with a perfect crystalline phase (Figure S5b). In the conventional route of synthesis of  $\text{La}_2\text{NiO}_4$ , similar results were obtained for its composition and crystalline transformation as the annealing temperature increased [38,45]. The BET surface area and pore diameter decreased with increase in the annealing temperature (Figure S5c,d). The SEM images showed that sintering occurred on the surface with particle agglomeration when the annealing temperature increased (Figure S6). We then evaluated the UOR activities of  $\text{La}_2\text{NiO}_4$  through a three-electrode configuration in 1 M KOH with 0.5 M urea under NIR light irradiation.  $\text{La}_2\text{NiO}_4$  annealed at  $800\text{ }^\circ\text{C}$  showed the best UOR activity (Figure S7), due to its large surface area and lack of sintering caused by high temperature calcination.

Since catalytic activities are commonly sensitive to valence states and the coordination environment of metal centers, X-ray photoelectron spectroscopy (XPS) was carried out to explore the chemical states of La, Ni and O in  $\text{La}_2\text{NiO}_4$ . As shown in Figure S8, the survey XPS spectrum clearly confirmed elemental composition of  $\text{La}_2\text{NiO}_4$ . As shown by the O 1s regions in Figure 2g, there were three peaks of  $\text{La}_2\text{NiO}_4$  that could be clearly identified, among which the peaks of 528.5 and 531.2 eV could be ascribed to metal oxygen bonds and surface-adsorbed water molecules, respectively. The peak located at 529.7 eV could be attributed to O atoms in the vicinity of an O vacancy. Figure 2h shows the Ni 2p spectra of  $\text{La}_2\text{NiO}_4$ , wherein the peak values of 851.6 eV and 854.7 eV in  $\text{La}_2\text{NiO}_4$  corresponded to the  $\text{Ni}^{2+} 2p_{3/2}$  and  $\text{Ni}^{3+} 2p_{3/2}$ , indicating the coexistence of  $\text{Ni}^{2+}$  and  $\text{Ni}^{3+}$  [36]. Nevertheless, due to the overlap of Ni  $2p_{3/2}$  and La  $3d_{3/2}$ , the ratio of  $\text{Ni}^{2+}$  and  $\text{Ni}^{3+}$  was still hard to calculate. However, the intensity of  $\text{Ni}^{3+}$  in  $\text{La}_2\text{NiO}_4$  was higher compared to that of  $\text{Ni}^{2+}$ , indicating that the prepared Ruddlesden–Popper  $\text{La}_2\text{NiO}_4$  would introduce partial oxygen vacancies, and more  $\text{Ni}^{2+}$  would be converted into  $\text{Ni}^{3+}$ . The  $\text{Ni}^{3+}$  was the active site that affected UOR activity [5], and, thus, would enhance the activity of UOR. For the La 3d (Figure 2i), there was no obvious peak position shift.

## 2.2. Photoelectrochemical Analysis of Catalysts

Photoelectrochemical measurements were conducted to evaluate the photoelectric properties of  $\text{La}_2\text{NiO}_4$ . In order to eliminate the current change caused by temperature, the photocurrent test under NIR light irradiation was carried out under low-power density light ( $100\text{ mW cm}^{-2}$ ) and in ice water bath (Figure S9). The results showed that NIR light could excite electrons without temperature inducing current change. The photocurrent density of the obtained  $\text{La}_2\text{NiO}_4$  was much higher than that of the sample prepared without the rGO template, indicating that the holey nanosheet structure of  $\text{La}_2\text{NiO}_4$  inherited from the rGO template was conducive to full contact between the electrode and the electrolyte and could enhance the absorption of light (Figure S4a). The active surface areas were further evaluated by electrochemical double-layer capacitance (Cdl) measurements (Figure S10). The Cdl value of  $\text{La}_2\text{NiO}_4$  electrode material prepared with the rGO template was calculated to be  $2.40\text{ mF cm}^{-2}$ , which was much higher than that of the electrode material prepared without the rGO template (Cdl =  $0.28\text{ mF cm}^{-2}$ ). The higher Cdl value of  $\text{La}_2\text{NiO}_4$  suggested a larger electrochemical active surface area of the porous and two-dimensional structure inherited from the rGO template. On the basis of the above results, the obtained  $\text{La}_2\text{NiO}_4$  was tested to be a superior catalyst for oxidation of urea.

### 2.3. UOR Activity

Given that the thermodynamic equilibrium potential shift from the 1.23 V vs. RHE of OER to the 0.37 V vs. RHE of the UOR favors the mass-production of hydrogen with a theoretical energy saving of ~70%, replacing the dreaded OER with UOR can result in energy efficient H<sub>2</sub> production [12]. We then investigated the photoelectrocatalytic activities of La<sub>2</sub>NiO<sub>4</sub> in 1 M KOH solution in the absence (OER) and presence of 0.5 M urea (UOR) by linear sweep voltammetry (LSV). As shown in Figure 3a, the remarkable peaks at about 1.42 V vs. RHE for the OER curves could be ascribed to the redox pair of Ni<sup>2+</sup>/Ni<sup>3+</sup>. A redox pair of symmetrical Ni<sup>2+</sup>/Ni<sup>3+</sup> was also found in the cyclic voltammetry (CV) curves (Figure S11) [7,31]. Meanwhile, the LSV curve showed that the UOR onset potential for La<sub>2</sub>NiO<sub>4</sub> was ~1.35 V vs. RHE. In comparison to the OER curve, recorded in the KOH electrolyte, the anodic current density of La<sub>2</sub>NiO<sub>4</sub> increased rapidly after adding urea, indicating that La<sub>2</sub>NiO<sub>4</sub> exhibited a high catalytic response activity for oxidation of urea. The NIR light irradiation could obviously accelerate the current density of UOR, with the application potential of 1.47 V vs. RHE current density of 2.00 mA cm<sup>-2</sup> under the NIR light irradiation, while the promotion effect on the OER curve was small, with a current density of 0.38 mA cm<sup>-2</sup> under NIR light and in the dark (Figure 3a). The photocurrent responses of the La<sub>2</sub>NiO<sub>4</sub> catalysts were also evaluated in 1 M KOH solution for OER and UOR processes under NIR light irradiation ( $\lambda > 800$  nm). As shown in Figure 3c, the photocurrent intensity of La<sub>2</sub>NiO<sub>4</sub> for the UOR process was around 50  $\mu$ A cm<sup>-2</sup>, which was much higher than that of the OER process (25  $\mu$ A cm<sup>-2</sup>). Furthermore, the UOR and OER kinetics of La<sub>2</sub>NiO<sub>4</sub> were investigated by the corresponding Tafel plots (Figure 3b). La<sub>2</sub>NiO<sub>4</sub> had a small Tafel slope of 79 mV dec<sup>-1</sup> for the UOR process. This value was substantially lower than that of the 165 mV dec<sup>-1</sup> needed for the OER process, demonstrating more beneficial catalytic kinetics of UOR than OER. Further studies of the La<sub>2</sub>NiO<sub>4</sub> electrode for UOR and OER kinetics by electrochemical impedance spectroscopy (EIS) were conducted. As shown in Figure 3d, the UOR process also had lower charge transfer resistance (R<sub>ct</sub>) values compared to OER, due to the increased rate of electron transfer between the electrode interface and the solute. The above results showed that replacing OER with UOR could greatly reduce the overpotential, and using La<sub>2</sub>NiO<sub>4</sub> as the photoanode could save energy to produce hydrogen.

Hydrogen production performances of the cathode were analyzed from the two anodes' half-reactions, UOR and OER, through a three-electrode system at an applied potential of 1.47 V vs. RHE. The current density was 0.96 mA cm<sup>-2</sup> for the UOR process, while only 0.08 mA cm<sup>-2</sup> for the OER process (Figure S12a). It was remarkable that the current densities of the two half-reactions were very stable, which meant that the La<sub>2</sub>NiO<sub>4</sub> catalyst showed excellent stability. The hydrogen production rates of the UOR and OER process were 9.75 and 0.55  $\mu$ mol cm<sup>-2</sup> h<sup>-1</sup>, respectively (Figure S12b). We integrated this electrolyzer with a commercial silicon solar cell to construct a solar-driven overall urea splitting system (Figure S13a). The *J-V* curves of 1 M KOH solution presented a high solar-to-hydrogen efficiency of 14.9% with 0.5 M urea, and 13.3% without urea [46–49], implying that a mild UOR, instead of the dreaded OER, could reduce the overpotential of hydrogen production at a smaller electrolytic voltage (Figure S13b). Similar measurements were performed using a Pt/C coated FTO electrode for comparison. The Pt/C coated FTO electrode showed negligible catalytic activity for UOR in the dark, while a significantly enhanced electrocatalytic performance could be observed after La<sub>2</sub>NiO<sub>4</sub> was coated on FTO (Figures S14a and S15). A smaller onset potential, higher current density and smaller Tafel slope of La<sub>2</sub>NiO<sub>4</sub> coating electrode were also observed for La<sub>2</sub>NiO<sub>4</sub>-coated FTO (Figure S14b). The hydrogen production of Pt/C electrode was negligible, which indicated that La<sub>2</sub>NiO<sub>4</sub> as the photoanode could replace noble metal to achieve efficient hydrogen production through UOR [3].

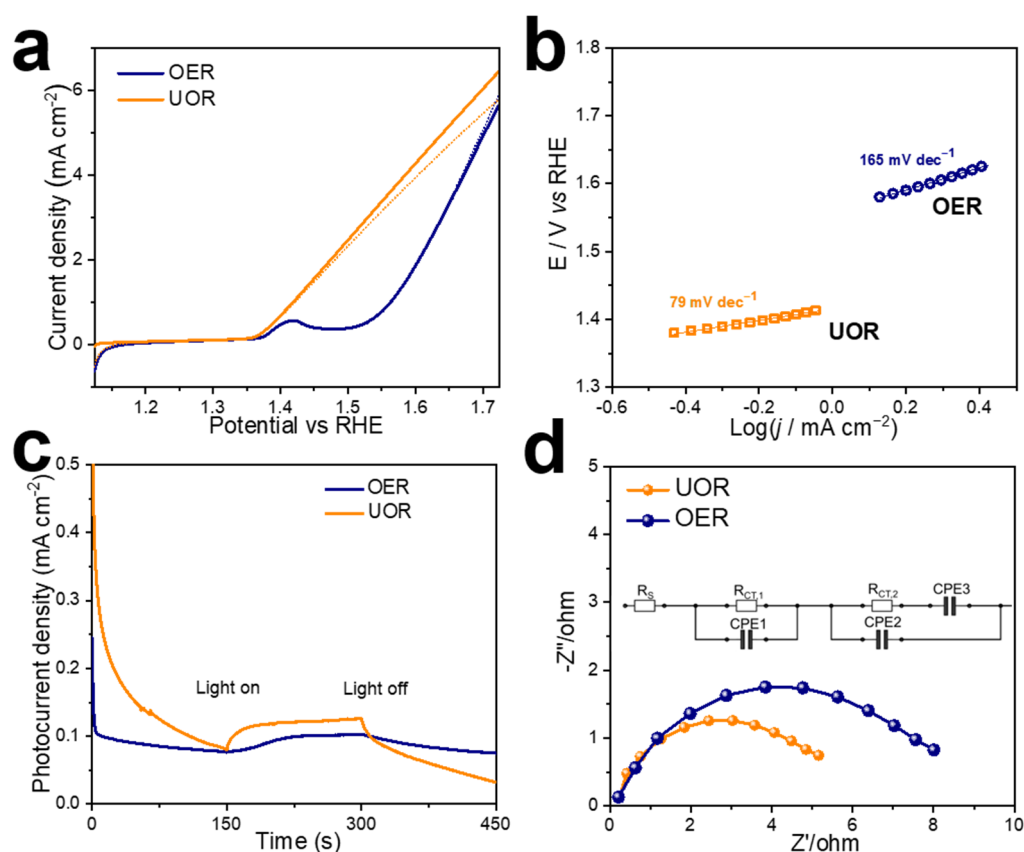


**Figure 3.** (a) Polarization curves for the UOR and OER under NIR light irradiation. The solid line and dotted line were under NIR and dark irradiation, respectively. (b) Tafel plots for the UOR and OER derived from (a). (c) Photocurrent response under NIR light irradiation with urea and without urea. (d) Nyquist plots with urea and without urea at open circuit voltage vs. Hg/HgO under NIR light irradiation.

The remarkable catalytic abilities observed above for the UOR under NIR light irradiation prompted us to explore the activities of  $\text{La}_2\text{NiO}_4$  as the electrode material under full spectrum light irradiation (Figure 4a), hence moving a step closer to practical applications. As shown in Figure 4b, the LSV curves of the  $\text{La}_2\text{NiO}_4$  electrode showed the same onset potential under different light source irradiations (UV-vis-NIR, visible, and NIR) in 1 M KOH with 0.5 M urea, and the current density under UV-vis-NIR irradiation was the highest. Furthermore, the UOR kinetics of  $\text{La}_2\text{NiO}_4$  were investigated through the corresponding Tafel plots and electrochemical impedance spectroscopy (EIS). The Tafel plot and charge transfer resistance ( $R_{ct}$ ) under UV-vis-NIR irradiation were comparatively lower than those under visible and NIR light (Figure 4c and Figure S16). Moreover, the photocurrent response plots (Figure S17) suggested that the photoanode excited more electrons for HER under UV-vis-NIR irradiation. The  $\text{H}_2$  generation rate and  $\Delta\text{TOC}$  of urea degradation under different light source irradiations were then recorded (Figure S18). Both the  $\text{H}_2$  generation rate and  $\Delta\text{TOC}$  of urea degradation were highest under UV-vis-NIR irradiation, compared to another light source irradiation, at  $22.76 \mu\text{mol cm}^{-2} \text{h}^{-1}$  and  $1750 \text{ mg/L}$ , respectively. The material stability was also important to estimate the long-term UOR activity of the photoelectrocatalyst. To assess the stability of the  $\text{La}_2\text{NiO}_4$  electrode, chronoamperometry ( $J-t$ ) measurements were performed at an applied voltage of 1.47 V vs. RHE. As shown in Figure 4d, superior catalytic stabilities, with negligible changes in current density, were maintained after 8h testing under various light irradiations, indicating the excellent durability of  $\text{La}_2\text{NiO}_4$  for the UOR process.

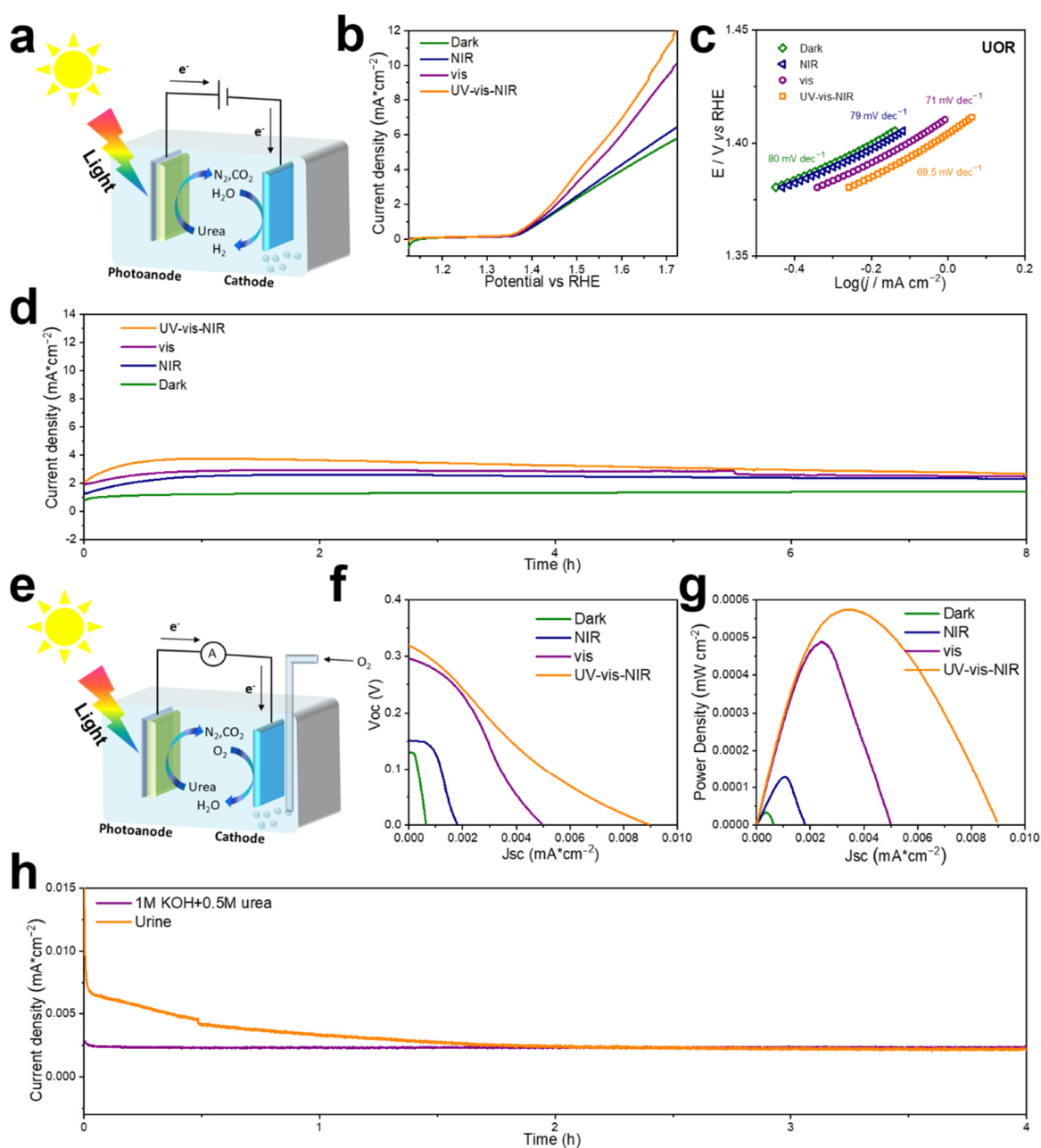
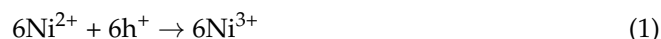


**Figure 4.** (a) Schematic diagram of the energy-saving hydrogen production process assisted by urea photoelectrocatalysis under various light source irradiations. (b) Polarization curves for the UOR of various light source irradiations. (c) Tafel plots for the UOR derived from (b). (d) Chronoamperometry responses recorded under various light source irradiations. Photoelectrocatalytic activity tests were performed in  $\text{N}_2$ -saturated 1 M KOH with 0.5 M urea electrolyte. (e) Illustration of a Photocatalytic Urea Fuel Cell (PUFC), based on  $\text{La}_2\text{NiO}_4$  photoanode and Pt counter electrode in  $\text{O}_2$ -saturated 1 M KOH with 0.5 M urea solution under various light source irradiations. (f) Polarization curves, and (g) corresponding power density curves of the PUFC device under different light sources in 1 M KOH with 0.5 M urea solution. (h) The current-time plots at 0.1 V output voltages in urea and human urine under NIR light irradiation. The catalyst loading is  $1 \text{ mg}\cdot\text{cm}^{-2}$  for the DUFC performance test.

Direct urea fuel cell (DUFC), as a device to produce electricity and purify urea/urine-rich wastewater at the same time, is of great significance for the integration of energy conversion and environmental treatment [9,11]. We evaluated the performance of a pho-

tocatalytic urea fuel cell in a two-electrode system. The process of continuous energy generation from PUFC is shown in Figure 4e. The  $\text{La}_2\text{NiO}_4$  photoanode generated electron hole pairs under exposure to light. The holes moved to the surface of  $\text{La}_2\text{NiO}_4$  to oxidize  $\text{Ni}^{2+}$  to  $\text{Ni}^{3+}$ , the active  $\text{Ni}^{3+}$  species then oxidized urea and was chemically reduced back to inactive  $\text{Ni}^{2+}$  [4]. The electrons that were transferred to external circuits providing a sustainable output for oxygen reduction reaction (ORR) at the cathode. The whole process is described as following:

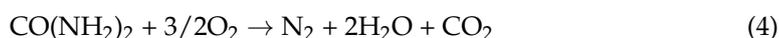
Photoanode:



Cathode:



Overall:



In order to further study the photocatalytic performances, the polarization curves of the PUFC under various light irradiations were collected (Figure 4f). It can be clearly observed that the PUFC showed the highest open-circuit voltage of 0.32 V and short-circuit current density of  $9.00 \mu\text{A cm}^{-2}$  under UV-vis-NIR irradiation, which displayed a higher energy compared to other light sources (Table S1). The same trends were found in the polarization and power curves (Figure 4f,g), with the maximum photovoltage response and output power density of  $0.575 \mu\text{W cm}^{-2}$  under the UV-vis-NIR light irradiation. Filling factor (FF) is commonly used to evaluate the performance of photocatalytic fuel cells, the FF value under NIR irradiation was 0.477 (Table S1), which was significantly larger than those of the other light sources [50]. The experimental results showed that the  $\text{La}_2\text{NiO}_4$  photoanode could process urea round-the-clock, which meant that it could not only efficiently convert urea into electricity in the daytime, but also continue the process under weak NIR light irradiation at night. The photoelectrochemical properties of the designed PUFC in urea solution with different concentrations were also investigated. Under NIR light irradiation, the current density, corresponding to the UOR polarization curves at a potential of 1.42 V vs. RHE, increased with increase of urea concentration, ranging from 0.1 to 0.5 M (Figure S19a). However, the relationship between the current density and urea concentration was nonlinear (Figure S19b), implying that excessive urea could not be oxidized in time by the  $\text{La}_2\text{NiO}_4$  photoanode [34]. The polarization curves also exhibited a similar trend under urea concentration ranging from 0.1 to 0.5 M, and the power curves demonstrated the corresponding output power density (Figure S20), and the short circuit current and maximum power density decreased with increase of urea concentration. Note that the UOR polarization curves (Figure S21) in urine were similar to the onset potential in urea solution, but the current density was reduced by an order of magnitude due to the lack of electrolytes. To further evaluate the PUFC performance of urine, the polarization curves (Figure S20k,i) showed open circuit voltage similar to that in urea solution under different light sources, which was still due to the influence of electrolytes, leading to a greatly reduced current density. However, the FF value in urine maintained a relatively high value of 0.411 under NIR light irradiation (Table S2), indicating the potential of using urine as fuel directly for PUFCs [10]. The durability of the PUFC was evaluated in 1 M KOH with urea and urine at 0.1 V output voltages, respectively (Figure 4h). The PUFC exhibited excellent stability within 240 min, without any major loss in performance in the urea solution. However, the current density in urine decreased sharply in the first 120 min and then tended to stabilize, possibly due to the interference of the complex components in urine [51].

## 2.4. UOR Activity

The mechanism of  $\text{La}_2\text{NiO}_4$ 's remarkable catalytic performance was also investigated by the adsorption and activation of urea on the surface of the  $\text{La}_2\text{NiO}_4$  catalyst (Figure 5). As shown in Figure 5a,b, the adsorption energy of urea on  $\text{La}_2\text{NiO}_4$  was  $-2.185$  eV, which indicated that the unique nanosheet structure of  $\text{La}_2\text{NiO}_4$  significantly enhanced the adsorption of urea on the catalyst surface. According to the electron localization function (ELF), there was a strong interaction between the N atom in urea and the La atom in  $\text{La}_2\text{NiO}_4$  (Figure 5c). Bader charge was analyzed to illustrate the electron transfer during the activation of the urea molecule. Urea transferred  $0.31$  e to  $\text{La}_2\text{NiO}_4$ , indicating that urea had a strong electron transfer effect with the catalyst surface. The theoretical results aligned well with our experimental evidence in the fact that the  $\text{La}_2\text{NiO}_4$  could efficiently adsorb and activate urea on the surface, resulting in excellent UOR activity.

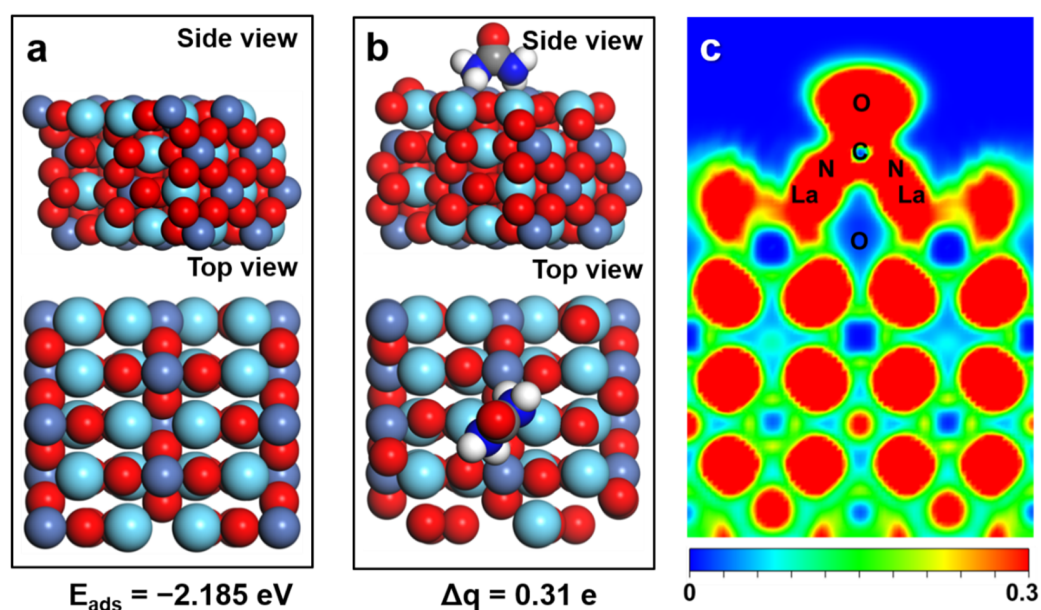


**Figure 5.** Optimization structures of (a)  $\text{La}_2\text{NiO}_4$  and (b) urea molecules adsorbed on  $\text{La}_2\text{NiO}_4$ , and urea adsorption energies and Bader charges. (c) Electron location function (ELF) for urea molecules adsorbed on  $\text{La}_2\text{NiO}_4$ . The green, navy blue, red, gray, blue, and white spheres represent La, Ni, O, C, N, and H atoms, respectively.

## 3. Materials and Methods

### 3.1. Synthesis of $\text{La}_2\text{NiO}_4$

The  $\text{La}_2\text{NiO}_4$ -precursor was deposited on the rGO by a simple chemical impregnation method. The  $\text{La}(\text{NO}_3)_3 \cdot 6\text{H}_2\text{O}$  (0.5 mmol),  $\text{Ni}(\text{NO}_3)_2 \cdot 6\text{H}_2\text{O}$  (0.25 mmol) and citric acid (2 mmol) were dissolved in 10 mL of deionized water and 20 mL ethanol, and then transferred into a 100 mL glass beaker. Subsequently, a certain amount of rGO was added into the mixture. After vigorous stirring and ultrasonic for 15 min, the mixture was maintained at  $70$  °C for 12 h under constant stirring. Excess  $\text{NH}_4\text{HCO}_3$  (2 g) was then added into the above mixture, and it placed in a  $50$  °C water bath, heated and dried to obtain the  $\text{La}_2\text{NiO}_4$  precursor. The  $\text{La}_2\text{NiO}_4$  precursor/rGO was treated at  $400$  °C for 2 h (heating rate:  $4$  °C  $\text{min}^{-1}$ ) and  $800$  °C for 2 h (heating rate:  $10$  °C  $\text{min}^{-1}$ ) under air atmosphere to obtain  $\text{La}_2\text{NiO}_4$ . All reagents were purchased from Aladdin (Shanghai, China) and were not further purified.

### 3.2. Characterization

Powder XRD patterns were obtained with Rigaku Dmax-3C Advance (Rigaku, Tokyo, Japan) X-ray diffractometer using Cu K $\alpha$  radiation at a wavelength of  $1.5406$  Å. Field emission scanning electron microscopy (FESEM) was conducted using a Hitachi S-4800 SEM

(Hitachi, Tokyo, Japan). Transmission electron microscopy (TEM) images and selected area electron diffraction (SAED) images were collected by using a JEOL 2010 TEM (JEOL, Tokyo, Japan). The XPS was performed with Perkin–Elmer PHI 5000 (Perkin–Elmer, Waltham, MA, USA) X-ray photoelectron spectroscopy. All of the values of binding energy were calibrated using C 1s = 284.8 eV as a reference. UV–vis diffuse reflectance spectra (UV–vis DRS) was obtained with an UV-2450 instrument (Shimadzu, Tokyo, Japan). The N<sub>2</sub> adsorption–desorption isotherms were collected by a TriStar II 3020 (micromeritics, Norcross, GA, USA) at 77 K, and all samples degassed at 423 K and 10<sup>−6</sup> Torr for 6 h. The Brunauer–Emmett–Teller (BET) approach was used to calculate the surface area. The zeta potential was measured on a Zetasizer Nano ZS90 (Malvern, UK).

### 3.3. Photoelectrochemical Measurement

All the photoelectrochemical measurements were performed on a CHI660E (Chenhua, Shanghai, China) electrochemical workstation using a three-electrode system. FTO-coated glass substrates (2 × 3 cm<sup>2</sup>) were cleaned sequentially with acetone, deionized water, and ethanol via sonication for 15 min. Subsequently, samples were loaded on the FTO through the doctor blade method, and the as-coated films were air-annealed at 200 °C for 2 h to form the working electrode. The mass loading of samples on FTO was about 1 mg cm<sup>−2</sup>. Hg/HgO (1 M KOH) and a commercial platinum foil (99.99%, 4 cm<sup>2</sup>) were used as the reference and counter electrodes, respectively. An airtight single cell was used as the reactor for PEC measurement. The electrolyte was purged with nitrogen (99.999%) to remove dissolved O<sub>2</sub> before testing. A 300 W xenon lamp was used as the UV–visible–NIR light (AM 1.5G, 1100 nm > λ > 300 nm), visible light (780 nm > λ > 420 nm) and near infrared light (λ > 800 nm) sources by using filters. The photocurrent density was detected in an aqueous solution containing 1 mol/L of KOH, 1 mol/L of KOH with 0.5 mol/L of urea or healthy people's fresh urine by linear sweep voltammetry (LSV) at a scan rate of 10 mV/s under different light sources. Electrochemical impedance spectroscopy (EIS) analyses were recorded in the 1 mol/L KOH, 1 mol/L KOH with 0.5 mol/L urea under different light at open-circuit voltage over the frequency range from 10<sup>6</sup> to 10<sup>−1</sup> Hz with an alternating current (ac) voltage of 5 mV. The electrochemical surface areas of different photoelectrodes were obtained by cyclic voltammetry (CV) measurements at scan rates of 10 mV/s, 20 mV/s, 30 mV/s, 40 mV/s, 50 mV/s, 60 mV/s, 70 mV/s, 80 mV/s, respectively, to estimate the electrochemical double layer. The transient photocurrent was measured at a bias voltage of 1.47 V vs. RHE.

### 3.4. Photoelectrocatalytic Activity Test

An H-cell and the electrolyte of 1 M KOH and 0.5 M urea were used for the UOR and HER tests. The H-cell was separated by an anion exchange membrane (AMI-7001). The cathode chamber electrolyte was purged with nitrogen (99.999%) to remove dissolved O<sub>2</sub> before testing. During the photoelectrocatalytic process, a constant potential (1.47 V vs. RHE) was applied on the working electrode. A 300 W xenon lamp was used as the UV–visible–NIR light (AM 1.5 G, 1100 nm > λ > 300 nm), visible light (780 nm > λ > 420 nm) and near infrared light (λ > 800 nm) sources. UOR and HER under UV visible light, visible light, near-infrared light and dark conditions were tested for 8 h, and the change of photocurrent within 8 h was recorded. An amount of 0.5 mL of sampled gas was used to analyze the hydrogen production rate using a gas chromatograph (GC9800 (N), Shanghai Ke Chuang Chromatograph Instruments Co. Ltd., Shanghai, China, TCD, with nitrogen as a carrier gas and a 5 A molecular sieve columns). The urea degradation rate was measured using Total organic carbon (TOC) content (vario TOC cube, elemental), and all solutions were diluted 10,000 times to obtain ΔTOC (urea) before testing.

### 3.5. Photocatalytic Fuel Cell Test

The PUFC performance was tested in a single cell with a two-electrode system using a CHI660E electrochemical workstation. The catalyst-coated FTO was used as the working

electrode, and the Pt foil was used as the auxiliary and reference electrode. The distance between the two electrodes was fixed at approximately 4 cm. A 300 W xenon lamp was used as the UV–visible–NIR light ( $AM\ 1.5\ G$ ,  $1100\ nm > \lambda > 300\ nm$ ), visible light ( $780\ nm > \lambda > 420\ nm$ ) and near infrared light ( $\lambda > 800\ nm$ ) sources. An aqueous solution of 1 mol/L KOH, 1 mol/L KOH with 0.5 mol/L urea or healthy people's fresh urine were used as the electrolyte, respectively. The change curve of open circuit voltage under different light sources was measured (Voc-t plots). The current–voltage (J–V) plots were collected to characterize the PFC performance with a scan rate of 1 mV/s. Each J–V plot was collected when the open circuit voltage was stabilized. A discharge test was conducted at 0.1 V for 4h, and the urea degradation rate was measured to obtain  $\Delta TOC$  (urea).

### 3.6. Computational Methods

All the spin theoretical simulations in our work were carried out on the Vienna ab initio Simulation Package (VASP) with version 5.4.1. The Generalized gradient approximation (GGA) with the Perdew–Burke–Ernzerhof (PBE) functional form was employed to evaluate the electron–electron exchange and correlation interactions while the projector augmented–wave (PAW) methods were implanted to represent the core–electron (valence electron) interactions. The GGA + U calculation was performed with the on-site Coulomb Repulsion U term on the Ni 3d and the Ueff (Ueff = U–J) value is 6.3 eV. Plane–Wave basis function was set with a kinetic cut–off energy of 550 eV. The ground–state atomic geometries were optimized by relaxing the force below 0.02 eV/Å and the convergence criteria for energy was set with the value of  $1.0 \times 10^{-5}$  eV/cell. A Monkhorst–Pack mesh, with the size of  $3 \times 3 \times 1$ , was employed to sample the surface Brillouin zone. The Gaussian method was employed for the both electronic structures and total energy of our models and stress/force relaxations. In order to simulate the interactions between molecules, van der Waal (vdw) interactions were included described by the DFT–D3 method of Grimme.

## 4. Conclusions

In summary, a two-dimensional porous Ruddlensden–Popper type nickel-based perovskite oxide  $La_2NiO_4$  was prepared using rGO as a template. Subsequent studies on UOR activity showed that the  $La_2NiO_4$  photoanode exhibited superior UOR performance under full spectrum solar irradiation, and, especially, the transient photocurrent could reach  $50\ \mu A\ cm^{-2}$  in urea solution under NIR light irradiation. The  $La_2NiO_4$  photoanode onset potential of UOR was only  $\sim 1.35\ V$  vs. RHE, which greatly increased the hydrogen production efficiency, compared to OER, which was attributed to the partial conversion of  $Ni^{2+}$  to  $Ni^{3+}$  caused by the oxygen deficiency in  $La_2NiO_4$ . The PUFC, constructed with  $La_2NiO_4$  as the photoanode, also showed excellent UOR activity and effective energy conversion under full spectrum solar irradiation. Moreover, the filling factor (FF) under NIR light was 0.477. This work shows that urea electrolyzers and photocatalytic fuel cells constructed from low-cost nickel-based perovskite oxides have potential for round-the-clock low energy hydrogen production and power generation by efficient utilization of solar energy.

**Supplementary Materials:** The following supporting information can be downloaded at: <https://www.mdpi.com/article/10.3390/catal13010053/s1>, Figure S1: The XRD pattern of the  $La_2NiO_4$  precursor/rGO; Figure S2: SEM of  $La_2NiO_4$  with rGO (a) and without rGO (b); Figure S3: (a) Nitrogen adsorption–desorption isotherms and (b) pore size distribution of  $La_2NiO_4$  with and without rGO added; Figure S4: (a) The UV–vis–NIR diffuse reflectance spectra and (b) UOR activity under NIR light of  $La_2NiO_4$  with and without rGO; Figure S5: (a) The XRD pattern (b) The UV–vis–NIR diffuse reflectance spectra (c) Nitrogen adsorption–desorption isotherms and (d) pore size distribution of  $La_2NiO_4$  annealed at 700 °C, 800 °C, 900 °C and 1000 °C, respectively; Figure S6: SEM images of  $La_2NiO_4$  annealed at 700 °C, 800 °C, 900 °C and 1000 °C, respectively; Figure S7: UOR activity under near-infrared light of  $La_2NiO_4$  annealed at 700 °C, 800 °C, 900 °C and 1000 °C, respectively; Figure S8: The XPS survey of  $La_2NiO_4$ ; Figure S9: Photocurrent response of near-infrared light in 1 M KOH and 0.5 M urea electrolyte under low-power density light ( $100\ mW\ cm^{-2}$ ) and low temperature ice water bath; Figure S10: (a,c), Cyclic voltammetry for  $La_2NiO_4$  with and without

rGO in a non-Faradaic region of the potential range from 0.82~1.02 V vs. RHE at scan rate from 10 to 80 mV s<sup>-1</sup> measured in 1.0 M KOH solution with 0.5 M urea. (b) and (d) The calculated Cdl. The current density at the potential of the 0.92 V vs. RHE plotted with the scan rates; Figure S11: Cyclic voltammetry (CV) curves of La<sub>2</sub>NiO<sub>4</sub> in 1 M KOH electrolyte with and without 0.5 M urea; Figure S12: (a) Chronoamperometry responses (j-t) of the 1 M KOH and 1 M KOH with 0.5 M urea at applied potential of 1.47 V vs. RHE under dark. (b) Hydrogen production at applied potential of 1.47 V vs. RHE under different reaction conditions. All processes were performed without special instructions at a concentration of 1 M KOH with 0.5 M urea; Figure S13: (a) A Schematic diagram showing commercial silicon solar cell-driven electrolysis of 1 M KOH with 0.5 M urea under sunlight. (b) Photocurrent density-potential curve (J-V) of the 1 M KOH or 1 M KOH with 0.5 M urea under UV-visible light and a commercial silicon solar cell under simulated AM 1.5-G 100 mW cm<sup>-2</sup> illumination; Figure S14: (a) UOR activity under dark of FTO, FTO coated with La<sub>2</sub>NiO<sub>4</sub> and 5% Pt/C, respectively. (b) Tafel plots for the UOR derived from (a); Figure S15: (a,b) Cyclic voltammetry for FTO and FTO coated with 5% Pt/C in a non-Faradaic region of the potential range from 0.82~1.02 V vs. RHE at scan rate from 10 to 80 mV s<sup>-1</sup> measured in 1.0 M KOH solution with 0.5 M urea. (c,d) The calculated Cdl. The current density at the potential of the 0.92 V vs. RHE plotted with the scan rates; Figure S16: Nyquist plots of various light sources in urea solution at open circuit voltage vs. Hg/HgO; Figure S17: Photocurrent response of various light sources in urea solution; Figure S18: ΔTOC (urea) and Hydrogen production rates of La<sub>2</sub>NiO<sub>4</sub> for the UOR at a constant applied potential of 1.47 V vs. RHE, respectively; Figure S19: (a) Polarization curves for the UOR under urea concentration ranging from 0.1 to 0.5 M under NIR light irradiation. (b) The photocurrent density at a potential of 1.47 V vs. RHE derived from (a); Figure S20: Polarization curves (J-V plots), and corresponding power density curves (J-P plots) of the PUFC device under urea concentration ranging from 0.1 to 0.5 M and human urine under various light source irradiations; Figure S21: Polarization curves for the UOR under human urine; Table S1: Performance parameters of PUFCs in 1 M KOH with 0.5 M urea exposed to different light sources irradiation; Table S2: Performance parameters of PUFCs under urea concentration ranging from 0.1 to 0.5 M and human urine exposed to NIR light irradiation.

**Author Contributions:** Conceptualization, X.C., G.L. and M.X.; methodology, Y.T., L.F. and D.P.; software, Y.T. and X.C.; validation, Y.T., L.F. and Y.S.; formal analysis, Y.T., G.L., X.C. and M.X.; investigation, T.H., J.M. and M.X.; resources, G.L. and M.X.; data curation, Y.T. and L.F.; writing—original draft preparation, Y.T. and M.X.; writing—review and editing, X.C. and G.L.; visualization, Y.T., L.F. and D.P.; supervision, M.X., X.C. and G.L.; project administration, G.L., M.X. and X.C.; funding acquisition, M.X., X.C. and G.L. All authors have read and agreed to the published version of the manuscript.

**Funding:** This research was funded by the “National Natural Science Foundation of China”, grant number 21876113, 21803038, 22176127, 22022608, 21261140333, the “National Key Research and Development Program of China”, grant number 2020YFA0211004, the “Shanghai Engineering Research Center of Green Energy Chemical Engineering, and the “111” Innovation and Talent Recruitment Base on Photochemical and Energy Materials”, grant number D18020.

**Data Availability Statement:** Not applicable.

**Acknowledgments:** We are grateful to the experimental officers at the Analysis and Testing Center, Shanghai Normal University, for their assistance with XRD, FE-SEM/EDX, TEM and XPS characterization.

**Conflicts of Interest:** The authors declare no conflict of interest. The funders had no role in the design of the study; in the collection, analyses, or interpretation of data; in the writing of the manuscript; or in the decision to publish the results.

## References

1. Li, J.; Li, J.; Liu, T.; Chen, L.; Li, Y.; Wang, H.; Chen, X.; Gong, M.; Liu, Z.P.; Yang, X. Deciphering and Suppressing Over-Oxidized Nitrogen in Nickel-Catalyzed Urea Electrolysis. *Angew. Chem. Int. Ed.* **2021**, *60*, 2–9. [[CrossRef](#)]
2. Van Damme, M.; Clarisse, L.; Whitburn, S.; Hadji-Lazaro, J.; Hurtmans, D.; Clerbaux, C.; Coheur, P.-F. Industrial and agricultural ammonia point sources exposed. *Nature* **2018**, *564*, 99–103. [[CrossRef](#)] [[PubMed](#)]
3. Li, F.; Chen, J.; Zhang, D.; Fu, W.-F.; Chen, Y.; Wen, Z.; Lv, X.-J. Heteroporous MoS<sub>2</sub>/Ni<sub>3</sub>S<sub>2</sub> towards superior electrocatalytic overall urea splitting. *Chem. Commun.* **2018**, *54*, 5181–5184. [[CrossRef](#)]
4. Forslund, R.P.; Mefford, J.T.; Hardin, W.G.; Alexander, C.T.; Johnston, K.P.; Stevenson, K.J. Nanostructured LaNiO<sub>3</sub> Perovskite Electrocatalyst for Enhanced Urea Oxidation. *ACS Catal.* **2016**, *6*, 5044–5051. [[CrossRef](#)]

5. Forslund, R.P.; Alexander, C.T.; Abakumov, A.M.; Johnston, K.P.; Stevenson, K.J. Enhanced Electrocatalytic Activities by Substitutional Tuning of Nickel-Based Ruddlesden–Popper Catalysts for the Oxidation of Urea and Small Alcohols. *ACS Catal.* **2019**, *9*, 2664–2673. [[CrossRef](#)]
6. Wang, L.; Ren, L.; Wang, X.; Feng, X.; Zhou, J.; Wang, B. Multivariate MOF-Templated Pomegranate-Like Ni/C as Efficient Bifunctional Electrocatalyst for Hydrogen Evolution and Urea Oxidation. *ACS Appl. Mater. Interfaces* **2018**, *10*, 4750–4756. [[CrossRef](#)]
7. Wang, G.; Wen, Z. Self-supported bimetallic Ni–Co compound electrodes for urea- and neutralization energy-assisted electrolytic hydrogen production. *Nanoscale* **2018**, *10*, 21087–21095. [[CrossRef](#)]
8. Lan, R.; Tao, S.; Irvine, J.T.S. A direct urea fuel cell—power from fertiliser and waste. *Energy Environ. Sci.* **2010**, *3*, 438–441. [[CrossRef](#)]
9. Senthilkumar, N.; Gnana Kumar, G.; Manthiram, A. 3D Hierarchical Core–Shell Nanostructured Arrays on Carbon Fibers as Catalysts for Direct Urea Fuel Cells. *Adv. Energy Mater.* **2018**, *8*, 1702207. [[CrossRef](#)]
10. Ranjani, M.; Senthilkumar, N.; Gnana Kumar, G.; Manthiram, A. 3D flower-like hierarchical NiCo<sub>2</sub>O<sub>4</sub> architecture on carbon cloth fibers as an anode catalyst for high-performance, durable direct urea fuel cells. *J. Mater. Chem. A* **2018**, *6*, 23019–23027. [[CrossRef](#)]
11. Zhu, X.; Dou, X.; Dai, J.; An, X.; Guo, Y.; Zhang, L.; Tao, S.; Zhao, J.; Chu, W.; Zeng, X.C.; et al. Metallic Nickel Hydroxide Nanosheets Give Superior Electrocatalytic Oxidation of Urea for Fuel Cells. *Angew. Chem. Int. Ed.* **2016**, *55*, 12465–12469. [[CrossRef](#)] [[PubMed](#)]
12. Han, W.K.; Wei, J.X.; Xiao, K.; Ouyang, T.; Peng, X.; Zhao, S.; Liu, Z.Q. Activating Lattice Oxygen in Layered Lithium Oxides through Cation Vacancies for Enhanced Urea Electrolysis. *Angew. Chem. Int. Ed.* **2022**, *61*, e202206050. [[CrossRef](#)] [[PubMed](#)]
13. Li, K.; Xu, Y.; He, Y.; Yang, C.; Wang, Y.; Jia, J. Photocatalytic Fuel Cell (PFC) and Dye Self-Photosensitization Photocatalytic Fuel Cell (DSPFC) with BiOCl/Ti Photoanode under UV and Visible Light Irradiation. *Environ. Sci. Technol.* **2013**, *47*, 3490–3497. [[CrossRef](#)] [[PubMed](#)]
14. Zhang, L.; Liang, C.; Guo, H.; Niu, C.-G.; Zhao, X.-F.; Wen, X.-J.; Zeng, G.-M. Construction of a high-performance photocatalytic fuel cell (PFC) based on plasmonic silver modified Cr-BiOCl nanosheets for simultaneous electricity production and pollutant removal. *Nanoscale* **2019**, *11*, 6662–6676. [[CrossRef](#)]
15. Chen, Q.; Li, J.; Li, X.; Huang, K.; Zhou, B.; Cai, W.; Shangguan, W. Visible-Light Responsive Photocatalytic Fuel Cell Based on WO<sub>3</sub>/W Photoanode and Cu<sub>2</sub>O/Cu Photocathode for Simultaneous Wastewater Treatment and Electricity Generation. *Environ. Sci. Technol.* **2012**, *46*, 11451–11458. [[CrossRef](#)]
16. Wu, Z.; Zhao, G.; Zhang, Y.; Liu, J.; Zhang, Y.-N.; Shi, H. A solar-driven photocatalytic fuel cell with dual photoelectrode for simultaneous wastewater treatment and hydrogen production. *J. Mater. Chem. A* **2015**, *3*, 3416–3424. [[CrossRef](#)]
17. Wu, J.; Tao, Y.; Zhang, C.; Zhu, Q.; Zhang, D.; Li, G. Activation of Chloride by Oxygen Vacancies-Enriched TiO<sub>2</sub> Photoanode for Efficient Photoelectrochemical Treatment of Persistent Organic Pollutants and Simultaneous H<sub>2</sub> Generation. *J. Hazard. Mater.* **2023**, *443*, 130363. [[CrossRef](#)]
18. Li, G.; Lian, Z.; Wang, W.; Zhang, D.; Li, H. Nanotube-confinement induced size-controllable g-C<sub>3</sub>N<sub>4</sub> quantum dots modified single-crystalline TiO<sub>2</sub> nanotube arrays for stable synergetic photoelectrocatalysis. *Nano Energy* **2016**, *19*, 446–454. [[CrossRef](#)]
19. Wu, L.; Li, F.; Xu, Y.; Zhang, J.W.; Zhang, D.; Li, G.; Li, H. Plasmon-induced photoelectrocatalytic activity of Au nanoparticles enhanced TiO<sub>2</sub> nanotube arrays electrodes for environmental remediation. *Appl. Catal. B Environ.* **2015**, *164*, 217–224. [[CrossRef](#)]
20. Li, G.; Lian, Z.; Li, X.; Xu, Y.; Wang, W.; Zhang, D.; Tian, F.; Li, H. Ionothermal synthesis of black Ti<sup>3+</sup>-doped single-crystal TiO<sub>2</sub> as an active photocatalyst for pollutant degradation and H<sub>2</sub> generation. *J. Mater. Chem. A* **2015**, *3*, 3748–3756. [[CrossRef](#)]
21. Li, G.; Jiang, B.; Li, X.; Lian, Z.; Xiao, S.; Zhu, J.; Zhang, D.; Li, H. C<sub>60</sub>/Bi<sub>2</sub>TiO<sub>4</sub>F<sub>2</sub> Heterojunction Photocatalysts with Enhanced Visible-Light Activity for Environmental Remediation. *ACS Appl. Mater. Interfaces* **2013**, *5*, 7190–7197. [[CrossRef](#)] [[PubMed](#)]
22. Wang, G.; Ling, Y.; Lu, X.; Wang, H.; Qian, F.; Tong, Y.; Li, Y. Solar driven hydrogen releasing from urea and human urine. *Energy Environ. Sci.* **2012**, *5*, 8215–8219. [[CrossRef](#)]
23. Xu, D.; Fu, Z.; Wang, D.; Lin, Y.; Sun, Y.; Meng, D.; Xie, T.F. A Ni(OH)<sub>2</sub>-modified Ti-doped α-Fe<sub>2</sub>O<sub>3</sub> photoanode for improved photoelectrochemical oxidation of urea: The role of Ni(OH)<sub>2</sub> as a cocatalyst. *Phys. Chem. Chem. Phys.* **2015**, *17*, 23924–23930. [[CrossRef](#)]
24. Zhang, L.; Ran, J.; Qiao, S.Z.; Jaroniec, M. Characterization of semiconductor photocatalysts. *Chem. Soc. Rev.* **2019**, *48*, 5184–5206. [[CrossRef](#)] [[PubMed](#)]
25. Liu, J.; Li, J.; Shao, M.; Wei, M. Directed synthesis of SnO<sub>2</sub>@BiVO<sub>4</sub>/Co-Pi photoanode for highly efficient photoelectrochemical water splitting and urea oxidation. *J. Mater. Chem. A* **2019**, *7*, 6327–6336. [[CrossRef](#)]
26. Zhu, B.; Liang, Z.; Zou, R. Designing Advanced Catalysts for Energy Conversion Based on Urea Oxidation Reaction. *Small* **2020**, *16*, e1906133. [[CrossRef](#)]
27. Dabboussi, J.; Abdallah, R.; Santinacci, L.; Zanna, S.; Vacher, A.; Dorcet, V.; Fryars, S.; Flonera, D.; Loget, G. Solar-assisted urea oxidation at silicon photoanodes promoted by an amorphous and optically adaptive Ni–Mo–O catalytic layer. *J. Mater. Chem. A* **2022**, *10*, 19769–19776. [[CrossRef](#)]
28. Tao, Y.; Chen, L.; Ma, Z.; Zhang, C.; Zhang, Y.; Zhang, D.; Pan, D.; Wu, J.; Li, G. Near-infrared-driven photoelectrocatalytic oxidation of urea on La-Ni-based perovskites. *Chem. Eng. J.* **2022**, *446*, 137240. [[CrossRef](#)]
29. Li, C.; Liu, Y.; Zhuo, Z.; Ju, H.; Li, D.; Guo, Y.; Wu, X.; Li, H.; Zhai, T. Local Charge Distribution Engineered by Schottky Heterojunctions toward Urea Electrolysis. *Adv. Energy Mater.* **2018**, *8*, 1801775. [[CrossRef](#)]

30. Periyasamy, S.; Subramanian, P.; Levi, E.; Aurbach, D.; Gedanken, A.; Schechter, A. Exceptionally Active and Stable Spinel Nickel Manganese Oxide Electrocatalysts for Urea Oxidation Reaction. *ACS Appl. Mater. Interfaces* **2016**, *8*, 12176–12185. [[CrossRef](#)]
31. Yu, Z.-Y.; Lang, C.-C.; Gao, M.-R.; Chen, Y.; Fu, Q.-Q.; Duan, Y.; Yu, S.-H. Ni–Mo–O nanorod-derived composite catalysts for efficient alkaline water-to-hydrogen conversion via urea electrolysis. *Energy Environ. Sci.* **2018**, *11*, 1890–1897. [[CrossRef](#)]
32. Tong, Y.; Chen, P.; Zhang, M.; Zhou, T.; Zhang, L.; Chu, W.; Wu, C.; Xie, Y. Oxygen Vacancies Confined in Nickel Molybdenum Oxide Porous Nanosheets for Promoted Electrocatalytic Urea Oxidation. *ACS Catal.* **2018**, *8*, 1–7. [[CrossRef](#)]
33. Kumar, A.; Liu, X.; Lee, J.; Debnath, B.; Jadhav, A.R.; Shao, X.; Bui, V.Q.; Hwang, Y.; Liu, Y.; Kim, M.G.; et al. Discovering Ultrahigh-Loading of Single-Metal-Atom via Surface Tensile-Strain for Unprecedented Urea Electrolysis. *Energy Environ. Sci.* **2021**, *14*, 6494. [[CrossRef](#)]
34. Geng, S.-K.; Zheng, Y.; Li, S.-Q.; Su, H.; Zhao, X.; Hu, J.; Shu, H.-B.; Jaroniec, M.; Chen, P.; Liu, Q.-H.; et al. Nickel ferrocyanide as a high-performance urea oxidation electrocatalyst. *Nat. Energy* **2021**, *6*, 904–912. [[CrossRef](#)]
35. Yin, W.-J.; Weng, B.; Ge, J.; Sun, Q.; Li, Z.; Yan, Y. Oxide perovskites, double perovskites and derivatives for electrocatalysis, photocatalysis, and photovoltaics. *Energy Environ. Sci.* **2019**, *12*, 442–462. [[CrossRef](#)]
36. Wang, H.; Wang, J.; Pi, Y.; Shao, Q.; Tan, Y.; Huang, X. Double Perovskite LaFe<sub>x</sub>Ni<sub>1-x</sub>O<sub>3</sub> Nanorods Enable Efficient Oxygen Evolution Electrocatalysis. *Angew. Chem. Int. Ed.* **2019**, *58*, 2316–2320. [[CrossRef](#)]
37. Li, G.; Zhang, Y.; Wu, L.; Wu, F.; Wang, R.; Zhang, D.; Zhu, J.; Li, H. An efficient round-the-clock La<sub>2</sub>NiO<sub>4</sub> catalyst for breaking down phenolic pollutants. *RSC Adv.* **2012**, *2*, 4822–4828. [[CrossRef](#)]
38. Tao, Y.; Wu, L.; Zhao, X.; Chen, X.; Li, R.; Chen, M.; Zhang, D.; Li, G.; Li, H. Strong Hollow Spherical La<sub>2</sub>NiO<sub>4</sub> Photocatalytic Microreactor for Round-the-Clock Environmental Remediation. *ACS Appl. Mater. Interfaces* **2019**, *11*, 25967–25975. [[CrossRef](#)]
39. Liu, J.; Jia, E.; Wang, L.; Stoerzinger, K.A.; Zhou, H.; Tang, C.S.; Yin, X.; He, X.; Bousquet, E.; Bowden, M.E.; et al. Tuning the Electronic Structure of LaNiO<sub>3</sub> through Alloying with Strontium to Enhance Oxygen Evolution Activity. *Adv. Sci.* **2019**, *6*, 1901073. [[CrossRef](#)]
40. Tian, J.; Sang, Y.; Yu, G.; Jiang, H.; Mu, X.; Liu, H. A Bi<sub>2</sub>WO<sub>6</sub>-Based Hybrid Photocatalyst with Broad Spectrum Photocatalytic Properties under UV, Visible, and Near-Infrared Irradiation. *Adv. Mater.* **2013**, *25*, 5075–5080. [[CrossRef](#)]
41. Cui, G.; Wang, W.; Ma, M.; Xie, J.; Shi, X.; Deng, N.; Xin, J.; Tang, B. IR-Driven Photocatalytic Water Splitting with WO<sub>2</sub>-Na<sub>x</sub>WO<sub>3</sub> Hybrid Conductor Material. *Nano Lett.* **2015**, *15*, 7199–7203. [[CrossRef](#)] [[PubMed](#)]
42. Jiang, W.; Bai, S.; Wang, L.; Wang, X.; Yang, L.; Li, Y.; Liu, D.; Wang, X.; Li, Z.; Jiang, J.; et al. Integration of Multiple Plasmonic and Co-Catalyst Nanostructures on TiO<sub>2</sub> Nanosheets for Visible-Near-Infrared Photocatalytic Hydrogen Evolution. *Small* **2016**, *12*, 1640–1648. [[CrossRef](#)] [[PubMed](#)]
43. Xin, Y.; Li, Z.; Wu, W.; Fu, B.; Zhang, Z. Pyrite FeS<sub>2</sub> Sensitized TiO<sub>2</sub> Nanotube Photoanode for Boosting Near-Infrared Light Photoelectrochemical Water Splitting. *ACS Sustain. Chem. Eng.* **2016**, *4*, 6659–6667. [[CrossRef](#)]
44. Peng, L.; Xiong, P.; Ma, L.; Yuan, Y.; Zhu, Y.; Chen, D.; Luo, X.; Lu, J.; Amine, K.; Yu, G. Holey two-dimensional transition metal oxide nanosheets for efficient energy storage. *Nat. Commun.* **2017**, *8*, 15139. [[CrossRef](#)]
45. Guo, C.; Zhang, X.; Zhang, J.; Wang, Y. Preparation of La<sub>2</sub>NiO<sub>4</sub> catalyst and catalytic performance for partial oxidation of methane. *J. Mol. Catal. A Chem.* **2007**, *269*, 254–259. [[CrossRef](#)]
46. Wang, Z.; Lin, Y.; Chen, R.; Liao, Q.; Zhu, X.; An, L.; He, X.; Zhang, W. A micro membrane-less photoelectrochemical cell for hydrogen and electricity generation in the presence of methanol. *Electrochim. Acta* **2017**, *245*, 549–560. [[CrossRef](#)]
47. Wang, S.; Chen, P.; Bai, Y.; Yun, J.-H.; Liu, G.; Wang, L. New BiVO<sub>4</sub> Dual Photoanodes with Enriched Oxygen Vacancies for Efficient Solar-Driven Water Splitting. *Adv. Mater.* **2018**, *30*, 1800486. [[CrossRef](#)]
48. Kim, M.; Lee, B.; Ju, H.; Kim, J.Y.; Kim, J.; Lee, S.W. Oxygen-Vacancy-Introduced BaSnO<sub>3-δ</sub> Photoanodes with Tunable Band Structures for Efficient Solar-Driven Water Splitting. *Adv. Mater.* **2019**, *31*, 1903316. [[CrossRef](#)]
49. Niu, S.; Jiang, W.-J.; Wei, Z.; Tang, T.; Ma, J.; Hu, J.-S.; Wan, L.-J. Se-Doping Activates FeOOH for Cost-Effective and Efficient Electrochemical Water Oxidation. *J. Am. Chem. Soc.* **2019**, *141*, 7005–7013. [[CrossRef](#)]
50. Pan, D.; Xiao, S.; Chen, X.; Li, R.; Cao, Y.; Zhang, D.; Pu, S.; Li, Z.; Li, G.; Li, H. Efficient Photocatalytic Fuel Cell via Simultaneous Visible-Photoelectrocatalytic Degradation and Electricity Generation on a Porous Coral-like WO<sub>3</sub>/W Photoelectrode. *Environ. Sci. Technol.* **2019**, *53*, 3697–3706. [[CrossRef](#)]
51. Schranck, A.; Marks, R.; Yates, E.; Doudrick, K. Effect of Urine Compounds on the Electrochemical Oxidation of Urea Using a Nickel Cobaltite Catalyst: An Electroanalytical and Spectroscopic Investigation. *Environ. Sci. Technol.* **2018**, *52*, 8638–8648. [[CrossRef](#)]

**Disclaimer/Publisher’s Note:** The statements, opinions and data contained in all publications are solely those of the individual author(s) and contributor(s) and not of MDPI and/or the editor(s). MDPI and/or the editor(s) disclaim responsibility for any injury to people or property resulting from any ideas, methods, instructions or products referred to in the content.